Microstructure and Conduction Electron Quantum Properties of Small Diamond Cubic α-Sn Nanocrystals Embedded in Cubic Boron Nitride Crystals

Sergiu V. Nistor, Leona C. Nistor, Mariana Stefan,* and Alexandra C. Joita

Read Online

ACCESS | Metrics & More | Article Recommendations | SI Supporting Information

ABSTRACT: The morphology, structure, composition, and conduction electron properties of quasi-spherical tin nanocrystals (NCs) of 2.5 nm average diameter, with unstrained, bulk-like α-Sn diamond cubic structure, observed in dark cubic boron nitride (cBN) crystallites, were determined by correlated analytical high-resolution scanning transmission electron microscopy and multifrequency electron spin resonance (ESR) investigations. The narrow Lorentzian ESR line with $g = 2.0028$ is attributed to the conduction ESR of the α-Sn NCs, consistent with the temperature- and frequency-independent small g-shift and intensity reduction under high temperature (950 °C) vacuum annealing when the α-Sn NCs are thermally dissolved in the host cBN crystallites. The ESR linewidth and line intensity *vs* temperature dependences recorded in the 20 to 295 K range are quantitatively described considering the presence of discrete, quantum confinement-induced conduction electron energy levels with $\Delta_{QC}/k_B = 125$ K separation, close to the theoretical value for conductive α-Sn NCs of 2.5 nm in diameter. The observed properties are tentatively explained with the predicted nanosize induced band-gap opening and change of band ordering from bulk α-Sn to small unstrained α-Sn NCs, resulting in a topological phase transition that also explains the predominantly s-like character of the conduction band electron orbitals.
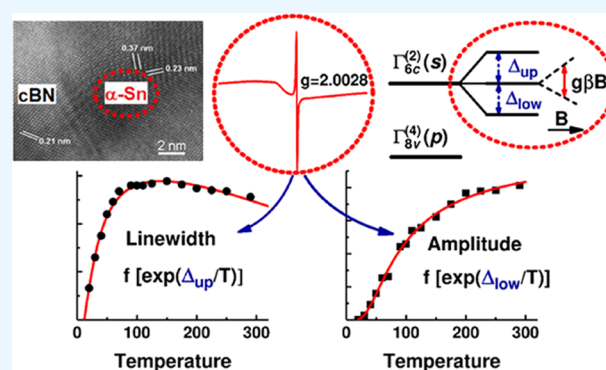
1. INTRODUCTION

Cubic boron nitride (cBN) with zinc blende structure is a wide band-gap (~6.4 eV) semiconductor, industrially prepared as a crystalline superhard powder by the temperature gradient method, at high pressure and high temperature (HP-HT), in a variety of alkali or alkali-earth B-N solvents to which additives and/or catalysts are added.[1−4] Despite the cBN outstanding properties,[4−7] the presence, distribution, and atomic properties of the impurities incorporated in its crystal lattice are little known. The main reason is the extreme difficulty of preparing enough large (mm-sized), good quality single crystals with controlled impurity content, as required for physical investigations.[8−11] With recent advances in microanalysis and microstructural techniques using electron beams,[12,13] it is now possible to investigate the presence, nature, and aggregation state of the impurities incorporated in the submillimeter-sized cBN crystallites found in large-sized commercial superabrasive powders. Thus, recent studies by analytical high-resolution scanning transmission electron microscopy/transmission electron microscopy [a-(HR)STEM/TEM], cathodoluminescence, ionoluminescence, and electron spin resonance (ESR) evidenced the presence and non-uniform distribution of certain impurities incorporated in the cBN crystallites.[14−17]

As reported here, tin (Sn) is such an impurity, which we found in dark BORAZON CBN Type 1 crystallites.

Bulk tin exhibits two phases, the high temperature white β-Sn phase with body-centered tetragonal symmetry (space group $I4_1/amd$) and metallic properties, stable at $T > T_c = 13.2$ °C,[18] and the low temperature gray α-Sn phase with diamond cubic structure [space group O_h^7 ($Fd\bar{3}m$)] stable at $T < T_c$, exhibiting specific electronic properties as a topological semimetal[19−21] or a direct zero-gap semiconductor.[22−25] Moreover, under strain, α-Sn can enter a Dirac semimetal or a strong topological insulator phase.[26,27] Ab initio and DFT calculations have shown that the α- and β-phases are close in energy,[28,29] which explains the difficulties in stabilizing the bulk α-Sn phase at $T > T_c$.[30−34] However, α-Sn NCs stable up to T_c ~ 200 °C, a property attributed to the interface and pressure/strain effects,[22] as well as to quantum confinement (QC),[35] were observed by transmission electron microscopy (TEM) in

annealed $Si_{1-x}Sn_x$ layers grown on Si(001) substrates[30,31,34] and in thick films of $Si_{1-x}Ge_x$.[32]

Up to now, physical investigations have been reported on very small free α-Sn NCs,[35] on large ($\sim$32 nm) α-Sn NCs embedded in thick layers of Ge,[32] and on smaller, mixed phase α/β-Sn NCs in Si layers.[30,34] To our knowledge, ESR investigations on α-Sn NCs were not reported so far. Very little is known about the undistorted α-Sn NCs, especially their electrical and magnetic properties, the available information resulting mainly from theoretical evaluations.[20,23,35−37]

We report here, from a-(HR)STEM/TEM and multi-frequency ESR investigations, the presence, morphology, structure, composition, and conduction electron properties of quasi-spherical α-Sn NCs with unstrained diamond cubic structure, of 2.5 nm average diameter, found in as-received commercial dark cBN crystallites prepared by HP-HT synthesis. Extensive information was obtained from the temperature evolution of the narrow, Lorentzian-shaped ESR line, called **Sn1**, with constant $g = 2.0028$ value in the 295 to 20 K temperature range, attributed to the conduction electron spin resonance (CESR) of the α-Sn NCs. Its linewidth and line intensity vs temperature variations could be quantitatively described considering the presence of a QC-induced conduction electron energy level sequence with average $\Delta_{QC}/k_B = 125$ K separation, a value in agreement with the theoretical predictions for α-Sn NCs of 2.5 nm average size.[38−40]

The observed behavior of the CESR linewidth and intensity, as well as its frequency- and temperature-independent g-value, are tentatively explained based on the theoretically predicted[23] QC-induced topological phase transition in small α-Sn NCs, resulting in band inversion and formation of an upper electron conduction band of mainly s-character, close to the Fermi level.

2. METHODS

2.1. Materials. *2.1.1. The Investigated Dark cBN Crystallites.* Samples of well-shaped dark cBN crystallites, with the largest size of up to $\sim$200 μm, were extracted from a batch of BORAZON CBN Type 1, 60/70 FEPA B251 commercial superabrasive powder. Their examination (Figure S1 in the Supporting Information) reveals that many of them exhibit triangular facets corresponding to (111) crystal planes. The powder X-ray diffraction (XRD) pattern (Figure S2 in the Supporting Information) confirms the presence of a high quality cubic BN single phase (space group $F43m$) with the lattice parameter $a_0 = 0.36157$ nm.[5] Thermal annealing treatment was also applied to samples of the as-received dark cBN crystallites. During such a treatment, pure fused silica tubes containing as-received dark cBN crystallites were connected to a turbo vacuum station ($P < 10^{-4}$ mbar) and inserted into an electronically controlled furnace. Its temperature was increased to 950 °C in about 0.5 h and further kept constant for about 4 h. At the end of the annealing period, the sample tube with the annealed cBN crystallites was removed from the furnace and cooled down to room temperature (RT), still under vacuum pumping, in less than 1 min. While the thermal treatment did not influence the dark color of the cBN crystallites, a deposit of white powder was formed at the cold end of the sample tube, where it exited the furnace. The largest part of the annealed and cooled cBN crystallites was transferred into clean pure fused silica sample tubes for further ESR measurements. Specimens for the a-(HR)STEM/TEM investigations were also extracted and prepared from the

annealed cBN crystallites and from the resulting white powder deposit.

2.2. Preparation. *2.2.1. Samples for the a-(HR)STEM/TEM Investigations.* The samples were prepared by crushing the cBN single crystallites (smaller than 200 μm) to induce cleaving and collecting the resulting tiny crystalline flakes dispersed in ethanol on lace carbon films. All images were obtained from the very thin parts of the cBN crystallites situated over the holes of the carbon films. Thus, one could avoid the influence of amorphous carbon grid bars on the HRTEM images or in the compositional analysis.

2.2.2. Samples for the ESR Measurements. To diminish the observed, rather strong microwave absorption, the cBN crystalline powder was inserted into narrow, one-end-closed pure fused silica sample tubes with thin walls, of 1 and 2 mm inner diameter, employed for the Q- and X-band ESR measurements in the 20 to 295 K and 90 to 295 K temperature ranges, respectively. During the ESR measurements at low temperatures, the open ends of the sample tubes were sealed off.

2.3. Characterization. *2.3.1. Microstructure and Composition Investigations.* Microstructure and composition investigations were performed with a JEOL JEM-ARM 200F field emission atomic resolution analytical electron microscope operating at 200 kV in both HRTEM and STEM modes. The microscope is equipped with a C_s probe corrector from CEOS, enabling a resolution of 0.08 nm in the STEM mode. In the HRTEM mode, the resolution of the microscope is 0.19 nm. The microscope is also equipped with a Gatan GIF Quantum SE Imaging Filter/EELS spectrometer for performing electron energy loss spectroscopy (EELS) composition determinations and a JEOL JED-2300T spectrometer for 2D elemental mapping by energy dispersive X-ray spectroscopy (EDS).

2.3.2. ESR Measurements. The ESR spectra were recorded in the X (9.8 GHz) and Q (34.1 GHz) microwave frequency bands using an ELEXSYS E580 Bruker spectrometer equipped with an ER4118X-MD5 X-band dielectric resonator and an ELEXSYS−E500Q Bruker spectrometer equipped with an ER5106QT/W Q-band probe head, respectively. Both spectrometers from NIMP-CetRESav (Magurele, Romania) were equipped with cryostats for low temperature ESR measurements, adapted for *in situ* monochromatic illumination using either laser diodes or light-emitting diodes as light sources.[41] The ESR spectral parameters were determined by numerical line deconvolution and fitting procedures using EasySpin v. 5.2.28 software.[42]

3. RESULTS

3.1. The Microstructural and Microanalytical Investigations. Previous (HR)TEM investigations revealed the presence of intrinsic extended defects in the dark cBN crystallites, such as dislocations, stacking faults, and micro-twins, as well as of small precipitates ($\sim$5 nm in average size), which could be formed by the aggregation of impurities, some of them at microtwin bands.[16] These impurities were most likely incorporated in the cBN crystallites during their HP-HT synthesis assisted by various additives.[3,5] We detail here the results of further a-(HR)STEM/TEM investigations concerning the nature and distribution of the impurities in the as-grown dark cBN crystallites and in the dark cBN crystallites vacuum-annealed at 950 °C, focusing mainly on the nature and structure of the observed nanometer-sized Sn precipitates.
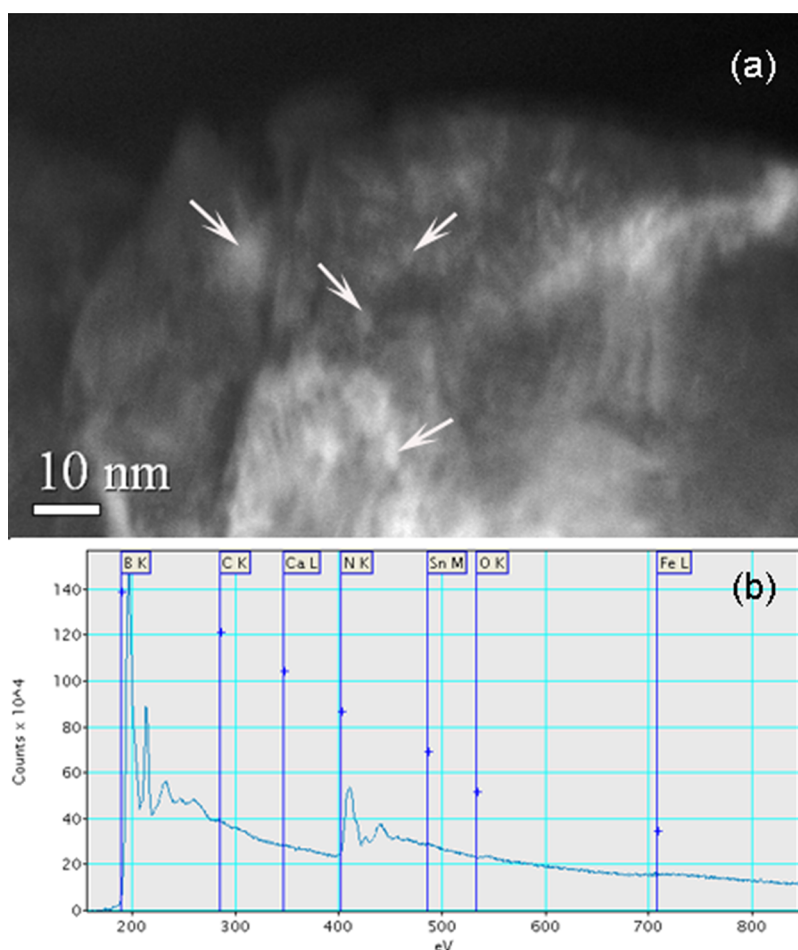
Figure 1. ADF-STEM image (a) and the EEL spectrum (b) generated from an area of (106×22) nm^2 of the investigated sample from image (a).

3.1.1. Impurity Analysis by STEM-EELS. To identify the nature and distribution of impurities, STEM-EELS analyses have been performed on a cBN sample prepared for (HR)TEM investigations. For the EELS measurements, the investigated specimen has to be very thin (thickness, <50 nm) to avoid multiple inelastic scattering effects. Moreover, for an accurate quantitative analysis, the specimen thickness t should be less than λ, the mean free path for inelastic scattering, preferably with $t/\lambda \leq 0.3$ to avoid multiple scattering effects.[43] Thus, from a specimen prepared for (HR)TEM investigations, we did choose from the cBN wedge-shaped crystalline flakes those with the thinnest edges. One should also prevent certain specimen orientations giving rise to strong diffraction conditions, which could affect the quantification of the EELS signals.

Our first goal was to identify the nature of the impurities present in the dark cBN sample. Figure 1a shows an ADF (annular dark field)-STEM image obtained on a very thin wedge edge of a cBN crystalline flake. Note that the ADF-STEM image is a dark field image; therefore, the background is black. On the other hand, the contrast of the image is dictated by the elemental composition of the specimen, the so-called Z-contrast, with the image intensity being proportional to Z^2, where Z is the atomic number. Therefore, for the BN compound, with $Z = 5$ for B and $Z = 7$ for N, the contrast in the STEM images is very weak, just a faint gray color, as it can be observed in Figure 1a on the very edge of the cBN crystalline flake.

The bright contrast in the ADF-STEM image of Figure 1a reveals the presence in this cBN crystalline flake of defects such as small precipitates (some indicated by arrows) and cleavage steps, while grooves appear in black contrast. We should mention that while cleavage steps and grooves might be produced during the specimen preparation for the (HR)TEM/STEM investigations, the precipitates resulting from impurity agglomeration are defects intrinsic to the examined cBN sample.[16]

Figure 1b presents the EEL spectrum generated by scanning an area of (106×22) nm^2 from the crystalline flake displayed in Figure 1a. The quantification of the EELS signals has been done with the GMS 2.0 software package using the power law background fitting at the edges of interest in the EEL spectrum and the Hartree−Slater method for the calculation of the ionization cross sections. The experimental parameters used for the EELS data acquisition were as follows: electron beam energy 200 keV; convergence semi-angle α = 7 mrad; collection semi-angle β = 49.02 mrad; electron probe size, 0.12 nm. The analyzed specimen was thin enough to avoid multiple inelastic scattering effects; therefore, the errors for the elemental quantification were in the range of 10%.

The resulting chemical composition values obtained from the quantification of the EEL spectrum from Figure 1b are presented in Table 1. The second column in the table shows the relative atomic ratio of two analyzed elements X and Y, i.e., the concentration of the element X being reported to the concentration of an element Y exhibiting the highest

Table 1. Chemical Composition Data and Identification of the Impurities in the Dark cBN Crystalline Flake Revealed in the ADF-STEM Image from Figure 1a[a]

element	atomic ratio (/N)	content (%)
B ($Z = 5$)	0.95 ± 0.13	41.75
C ($Z = 6$)	0.08 ± 0.01	3.55
Ca ($Z = 20$)	0.02 ± 0.01	0.71
N ($Z = 7$)	1.00 ± 0.00	43.92
Sn ($Z = 50$)	0.06 ± 0.01	2.49
O ($Z = 8$)	0.08 ± 0.01	3.40
Fe ($Z = 26$)	0.10 ± 0.01	4.17

[a]The first column gives the elements for which the edges were identified in the EEL spectrum from Figure 1b, while the corresponding atomic numbers Z are indicated between brackets. The second column shows the relative atomic ratio of elements X and N. The third column gives the calculated percent content of each element in the investigated area.

Figure 2. ADF-STEM images at low (a) and high (b) magnifications showing nanosized precipitates embedded in the dark cBN crystallite; z1 to z5 mark the particular positions on the ADF-STEM images where the electron beam spot was placed for the EELS analyses.

concentration in the quantification process, which in the present case is nitrogen. In this way, provided that the same integration window is employed in the calculations, the computed cross-section errors tend to cancel and artifacts, including thickness and diffraction contrast, are corrected.

One can see that the impurity atoms detected by EELS in the very thin analyzed area of the dark cBN crystalline flake are C, Ca, Sn, O, and Fe. Among them, C, O, Ca, and Fe are commonly found in cBN, and they were detected in different cBN crystalline powders prepared by HP-HT synthesis in the presence of various additives or catalysts.[3] Detecting Sn in the dark cBN sample was surprising. It is worth mentioning that the name "Borazon" for cBN has been first proposed by Wentorf,[44] who also mentioned the use of metallic Sn as a catalyst for the cBN synthesis.[1] This could explain its presence in the presently investigated dark cBN crystallites. Note that the metallic impurities, especially Sn, have a significant larger Z than B and N. Hence, it is very likely that the precipitates seen in the ADF-STEM image of Figure 1a as white dots contain tin.

3.1.2. Identification by STEM-EELS of the Nature of the Precipitates in the Dark cBN Crystallites. While examining many of the ADF-STEM images obtained on thin crystalline flakes from the dark cBN sample, we observed, only in a few of them, the presence of nanosized precipitates. This situation is illustrated in Figure 2, which presents ADF-STEM images obtained at low (a) and high (b) magnifications.

The ADF-STEM image at low magnification from Figure 2a shows a large area at the edge of a cBN crystalline flake where several precipitates, incorporated in the cBN matrix, are revealed by the bright Z-contrast. The larger the precipitates, the brighter they appear. At this low magnification, mainly the larger precipitates are observed. We have also measured in Figure 2a the diameter of several precipitates. The precipitate marked with z1 has a diameter $d = (37 \pm 2)$ nm, while the one marked with z3 has $d = (23 \pm 2)$ nm. Most of the large precipitates appearing in Figure 2a are in this dimension range. On the other hand, the small precipitates (<5 nm) are hardly visible in the low magnification ADF-STEM images. For the few small precipitates observed in Figure 2a, we measured diameters of $[(6{-}8) \pm 2]$ nm.

In Figure 2a, the cBN crystalline flake matrix exhibits a rather weak dull contrast. Only some cleavage steps can be observed, since the thicker the cBN crystallite flake, the
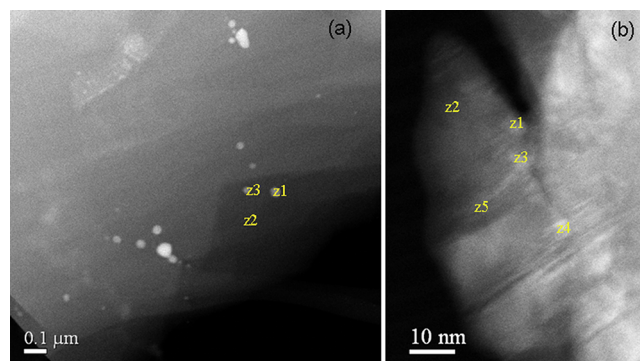
brighter is the contrast in the ADF-STEM image. Note that most of the large precipitates appear in Z-contrast in the thicker parts of the wedge-shaped cBN crystalline flake. On the ADF-STEM image from Figure 2a, z1 to z3 mark the positions on the thinner edge of the cBN crystalline flake where the scanning electron beam was stopped to acquire the EEL spectra of the two rather large precipitates (z1 and z3) and of the zone outside them (z2). However, in all three cases, the sample was too thick to perform a correct quantification of the EELS signals. Nevertheless, we emphasize that Sn has been detected on z1 and z3, i.e., on precipitates, but not on the zone z2 outside the precipitates.

To analyze the nature of the small precipitates ($d < 5$ nm) previously observed by TEM,[16] we had to perform STEM at much higher magnifications. Figure 2b presents a high magnification ADF-STEM image obtained on the thin edge of another cBN crystalline flake. Here, small precipitates, marked as z1, z3, and z4, can be observed in Z-contrast. Of course, being so small, their contrast is weak, but they are still visible. The diameters of these precipitates measured in Figure 2b are (2.30 ± 0.09) nm for the precipitate z1, (2.70 ± 0.09) nm for the precipitate z3, and (2.03 ± 0.09) nm for the z4 precipitate. The EEL spectra were acquired with the electron beam placed on these precipitates and on zones with no precipitates (marked as z2 and z5). In all analyzed zones, the specimen was thin enough to perform a correct quantification of the EEL spectra with errors of 10%. Examining the quantification results presented in Table 2, one finds that the impurities detected in the dark cBN crystalline flake are not uniformly distributed between the analyzed zones z1 to z5 presented in Figure 2b.

Among them, Sn was detected only in the precipitates (z1, z3, and z4) and not in the zones outside the precipitates (z2 and z5). Therefore, one concludes that the nanosized precipitates contain Sn atoms, which explains their bright Z-contrast in the ADF-STEM images.

3.1.3. The Structure of the Tin Precipitates in the Dark cBN Crystallites Obtained by (HR)TEM. To identify the structure of the Sn precipitates incorporated in the cBN matrix, it is necessary to perform (HR)TEM investigations with the cBN crystalline sample oriented along a specific zone axis. Thus, we tilted in the electron microscope the cBN crystalline flake presented in the ADF-STEM image from Figure 2a, until the electron beam was aligned along the [011] zone axis. Figure 3a presents a low magnification TEM image obtained in

Table 2. Composition Analysis of the Nanosized Precipitates Incorporated in the Dark cBN Crystalline Flake, As Observed in the ADF-STEM Image from Figure 2b

element	atomic ratio (/N) for z1 (precipitate)	atomic ratio (/N) for z2	atomic ratio (/N) for z3 (precipitate)	atomic ratio (/N) for z4 (precipitate)	atomic ratio (/N) for z5
B (Z = 5)	0.92 ± 0.13	0.91 ± 0.13	0.90 ± 0.13	0.99 ± 0.14	0.89 ± 0.13
C (Z = 6)	0.01 ± 0.01	0.00 ± 0.01	0.00 ± 0.01	0.00 ± 0.01	0.00 ± 0.01
Ca (Z = 20)	0.01 ± 0.01	0.01 ± 0.01	0.01 ± 0.01	0.00 ± 0.01	0.02 ± 0.01
N (Z = 7)	1.00 ± 0.00	1.00 ± 0.00	1.00 ± 0.00	1.00 ± 0.00	1.00 ± 0.00
Sn (Z = 50)	0.01 ± 0.01	0.00 ± 0.01	0.01 ± 0.01	0.02 ± 0.01	0.00 ± 0.01
O (Z = 8)	0.06 ± 0.01	0.01 ± 0.01	0.04 ± 0.01	0.06 ± 0.01	0.00 ± 0.01
Fe (Z = 26)	0.08 ± 0.01	0.05 ± 0.01	0.05 ± 0.01	0.15 ± 0.02	0.04 ± 0.01
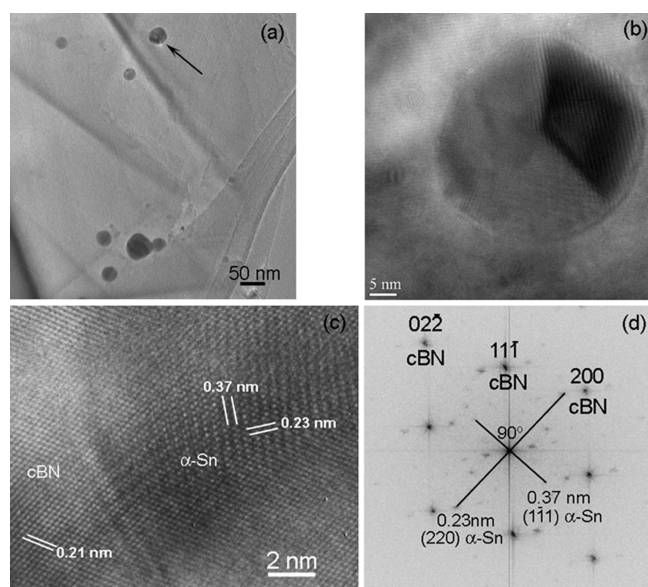
Figure 3. Low magnification TEM image (a) and HRTEM images (b, c) along the [011] zone axis, showing Sn precipitates embedded in a dark cBN crystalline flake; (d) FFT of image (b) revealing periodicities associated with both the cBN crystal matrix and α-Sn precipitate.

diffraction contrast along the [011] zone axis of cBN, revealing precipitates of different sizes embedded in the matrix of the cBN crystalline flake. The nanosized crystalline precipitates appear in dark contrast.

The arrow in Figure 3a indicates a large precipitate, the one that has been marked with z1 in the ADF-STEM image of Figure 2a. On this Sn precipitate we performed HRTEM investigations. The low magnification HRTEM image from Figure 3b illustrates the Sn precipitate embedded in the cBN crystalline matrix, which has a nearly spherical shape and an average diameter of 37 nm. Moreover, it is crystalline, exhibiting facets and Moiré fringes.

Figure 3c presents an HRTEM image at a higher magnification, revealing a portion of this Sn precipitate where atomic resolution has been obtained. The measured distances between the lattice fringes indicated in Figure 3c are 0.37 and 0.23 nm, which correspond, respectively, to the distances between the (111) and (220) lattice planes of the α-Sn phase with diamond cubic structure ($a_0 = 0.6489$ nm, space group $Fd\overline{3}m$[45]). One should point out that these interplanar spacings do not exist in the β-Sn phase with tetragonal structure.[46] In Figure 3c, the interplanar distance of 0.21 nm for the (111) planes of the cBN matrix is also marked. The crystal structure of the Sn precipitate could be more accurately

determined from the fast Fourier transform (FFT) image generated by the HRTEM image from Figure 3b. The result is presented in Figure 3d, where the large dark spots represent the cBN crystal periodicities along the [011] zone axis, while the faint small spots represent the periodicities associated with the Sn precipitate and with the Moiré fringes generated between the cBN crystalline flake and the α-Sn NCs of similar structures but very different lattice constants. The cBN lattice periodicities are used as a calibration to further calculate the periodicities of the nanocrystalline Sn precipitate. The dark lines are drawn to guide the eye.

The measured periodicities for the nanocrystalline Sn precipitate are $d_{1-11} = 0.380$ nm and $d_{220} = 0.226$ nm, while the measured angle between the two spots (reflections), labeled 0.38 and 0.23 nm in Figure 3d, is 90°. The values of the interplanar spacings d_{hkl} as well as the measured angle between the two reflections are consistent with the diamond cubic structure of α-Sn.

It is worth mentioning that α-Sn NCs of comparable dimensions embedded in a Ge matrix have been previously reported.[32] It has been also shown that although the α-Sn precipitates are formed at high temperatures, their diamond structure is preserved at RT if they are embedded in matrices of a similar structure such as Ge or Si.[31,32,34] On the other hand, our STEM-EELS and HRTEM experiments demonstrate that the diamond structure of the nanocrystalline precipitates of α-Sn is also preserved at RT when incorporated in matrices of cBN crystallites with a cubic zinc blende structure, similar to the diamond structure, except that the C atoms are alternatively replaced by B and N atoms.

3.1.4. Size Distribution of the Small α-Sn NCs Incorporated in the Dark cBN Crystallites. According to the ADF-STEM and (HR)TEM images, the dimensions of the α-Sn NCs belong mainly to two size classes, small (<5 nm) and large (>20 nm). It is worth mentioning that according to ref 35, the small Sn NCs exhibit a better stability in the α-Sn diamond cubic structure. A more accurate size distribution of the small α-Sn NCs incorporated in the cBN crystallites was obtained by examination of the TEM images at high magnifications. Figure 4a presents such a higher magnification TEM image of the upper part of the cBN crystalline flake, previously presented in the low magnification TEM image of Figure 3a. At this higher magnification, it reveals a rather large number of small precipitates/NCs and two large ones incorporated in the cBN crystalline matrix. The measured dimensions of the large NCs are (37.35 ± 0.45) and (22.50 ± 0.45) nm.

The size distribution of the small NCs is given in the histogram from Figure 4b, obtained by measuring the diameter of the 79 such NCs from Figure 4a. The size distribution
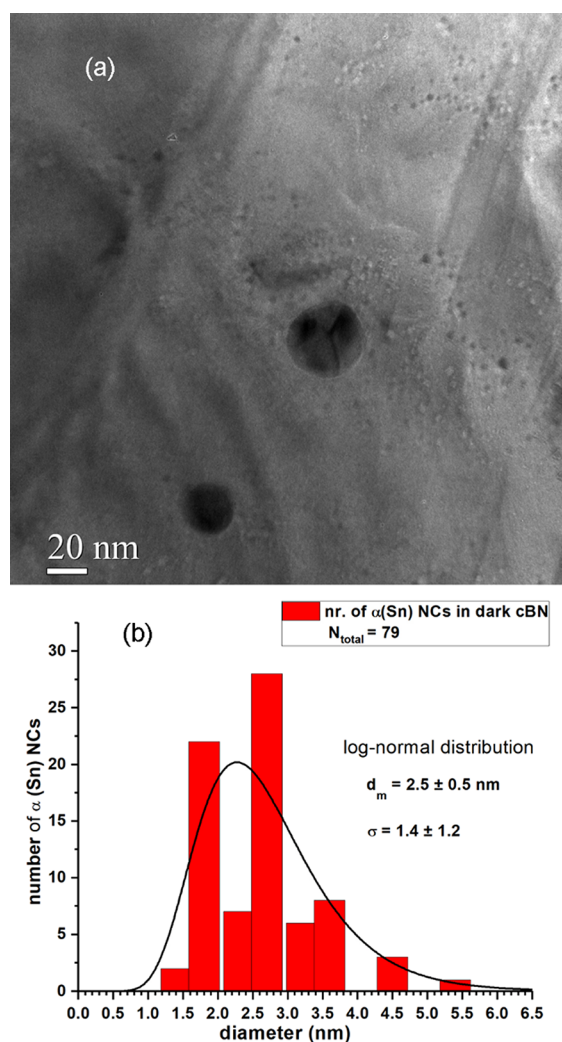
Figure 4. High magnification TEM image (a) revealing the α-Sn NCs incorporated in a dark cBN crystalline flake. (b) Histogram showing the size distribution of the 79 small NCs.

histogram has been fitted with a log-normal function. From this fit, we determined the two parameters of the log-normal function: the statistical mean particle diameter $d_m = (2.5 \pm 0.5)$ nm, which is very close to the calculated 2.54 nm average diameter and the geometrical standard deviation $\sigma = 1.4 \pm 1.2$. As will be further shown, these small α-Sn NCs are responsible for the conduction electron quantum properties observed by ESR. For simplicity, in the further interpretation of the ESR data, we will use the value of 2.5 nm for the average dimension of the small α-Sn NCs.

3.1.5. Dispersion of the Sn Precipitates in the Host cBN Crystallites Vacuum-Annealed at 950 °C Evidenced by STEM-EELS. To disperse the tin precipitates incorporated as α-Sn NCs in the cBN lattice host, crystallites of the as-received cBN were annealed for 4 h at 950 °C in vacuum, as detailed in Section 2.1. The resulting white powder deposited in the cold part of the fused silica tube, on the inner side of its walls, was removed and studied by (HR)TEM, electron diffraction, and elemental EDS mapping. As detailed in the Supporting Information, the residual white powder consisted of crystalline SnO_2 with tetragonal structure and crystallite dimensions between 5 and 25 nm (see Figures S3 and S4 from the Supporting Information). It means that such Sn precipitates,

previously observed in the as-received cBN crystallites, were at least partly dissolved/dispersed and expelled from the cBN crystalline matrix by annealing.

The distribution of the impurities in the thermally annealed dark cBN crystals has been further investigated by STEM-EELS. Figure 5 shows the ADF-STEM image of the edge of a
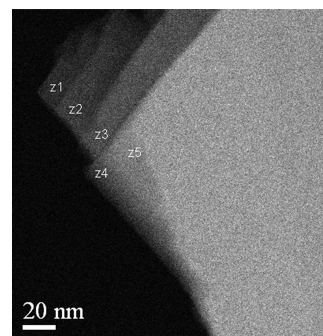
Figure 5. ADF-STEM image of a crystalline flake obtained from the dark cBN sample annealed in vacuum at 950 °C; z1 to z5 mark the particular positions where the electron beam spot was placed to perform the EELS analyses.

crystalline flake from the annealed dark cBN specimen. The Z-contrast of the image is rather even, revealing only several cleavage steps of different thicknesses, which probably occurred during the preparation of specimens for TEM observation. Unlike the ADF-STEM images from Figure 2, the examination of Figure 5 reveals that no Sn aggregates/precipitates are visible in Z-contrast in the observational magnification range. It confirms that by thermal treatment, the Sn precipitates are largely dissolved in the lattice host, with the resulting Sn atoms being expelled from the cBN crystals. Further, we chose on the cleavage steps different positions marked as z1 to z5, where the corresponding EEL spectra were acquired. In all analyzed zones, the specimen was thin enough for a correct quantification of the EEL spectra with 10% errors. Table 3 gives the results of EELS analyses from spots z1 to z5.

According to the data presented in Table 3 and Figure 5, the annealing of the dark cBN crystals at 950 °C results in the thermally induced dispersion of the α-Sn NCs in the as-received cBN crystals. Further, during the annealing, the dispersed Sn atoms migrate to the surface of the cBN crystals and react with the oxygen atoms, forming SnO_2 deposited on the colder part of the enclosing fused silica tube, while the remaining Sn impurities are redistributed non-uniformly in the cBN crystal. One can thus explain the observed non-uniform distribution of the remaining Sn atoms in the annealed cBN, as revealed in Table 3.

3.2. The ESR Investigations and Resulting Spectral Properties. ESR spectroscopy, which has been extensively employed in investigating the properties of unpaired electrons trapped at lattice point defects in solids,[41,47,48] has also been used to study the conduction electron spin resonance of metal colloids incorporated in insulating or semiconductor crystals.[38,39,49,50] To understand the electron properties of the α-Sn NCs identified by TEM in the dark cBN crystallites, we performed ESR measurements over a broad temperature range, with the results being further analyzed in correlation with the microstructure and microanalysis data obtained from the same samples, as well as with published results of first principle

Table 3. Nature and Concentration of Impurities in the Edge Zone of an Annealed cBN Crystalline Flake Determined in the Positions Marked as z1 to z5 on the ADF-STEM Image from Figure 5

element	atomic ratio (/N) for z1	atomic ratio (/N) for z2	atomic ratio (/N) for z3	atomic ratio (/N) for z4	atomic ratio (/N) for z5
B ($Z = 5$)	0.92 ± 0.13	0.84 ± 0.12	0.85 ± 0.12	0.88 ± 0.13	0.86 ± 0.12
C ($Z = 6$)	0.00 ± 0.01	0.01 ± 0.01	0.05 ± 0.01	0.04 ± 0.01	0.01 ± 0.01
Ca ($Z = 20$)	0.02 ± 0.01	0.03 ± 0.01	0.03 ± 0.00	0.02 ± 0.01	0.01 ± 0.01
N ($Z = 7$)	1.00 ± 0.00	1.00 ± 0.00	1.00 ± 0.00	1.00 ± 0.01	1.00 ± 0.00
Sn ($Z = 50$)	0.05 ± 0.01	0.04 ± 0.01	0.00 ± 0.01	0.00 ± 0.01	0.00 ± 0.01
O ($Z = 8$)	0.06 ± 0.01	0.00 ± 0.01	0.06 ± 0.01	0.09 ± 0.01	0.00 ± 0.01
Fe ($Z = 26$)	0.02 ± 0.03	0.10 ± 0.02	0.04 ± 0.01	0.05 ± 0.01	0.04 ± 0.01
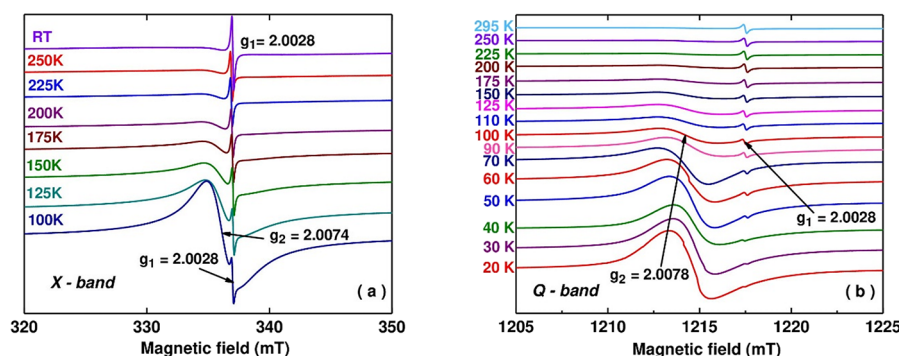
Figure 6. Sequences of the ESR spectra of the as-received dark cBN crystallites recorded as a function of temperature: (a) in the X (9.45 GHz) and (b) Q (34.125 GHz) frequency bands. The effective g_1 and g_2 values correspond to the **Sn1** and **Sn2** component lines, respectively.
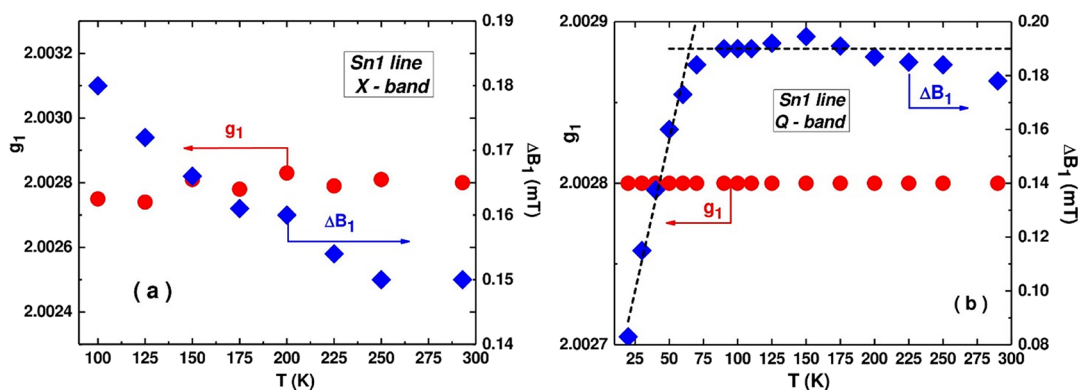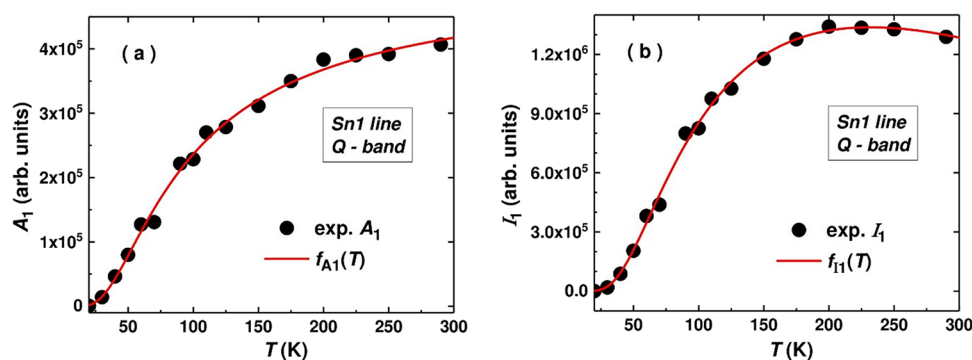

Figure 7. Temperature-induced variation of the g-factor (left side ordinates, dots) and derivative peak-to-peak linewidth (ΔB_1) (right side ordinates, diamonds) of the **Sn1** line, determined in the (a) X (9.45 GHz) and (b) Q (34.125 GHz) frequency bands. The dashed lines, described by $\Delta B_1 = 0.044 + 0.0022T$ for $T < 60$ K and $\Delta B_1 = 0.19$ mT for $T > 60$ K, serve as a guide for the eye in discussing the data *vs* temperature dependence.

quantum calculations of the α-Sn NCs structure and electronic properties.

The ESR spectra of the as-received dark cBN crystallites recorded in the X and Q frequency bands, from RT down to 100 and 20 K, respectively (Figure 6), consist of two main component lines, namely, a narrow, symmetrical line, called **Sn1**, and a broader asymmetrical one at lower magnetic fields, called **Sn2**. The **Sn1** line exhibits a Lorentzian shape in both X and Q frequency bands, with the same temperature-independent $g = 2.0028 \pm 0.0001$ value. In the case of the broader **Sn2** line centered at lower magnetic fields ($g \sim 2.0078$), the temperature-dependent lineshape reflects the presence of at least two overlapping broad component lines.

The ESR spectra of the dark cBN crystallites subjected to vacuum annealing at 950 °C have been also recorded. The resulting spectra recorded in the X- and Q-bands at RT (Figures S5a,b in the Supporting Information) and at 100 K

(Figures S5c,d in the Supporting Information) exhibit a strong drop in the intensity of the narrow **Sn1** line in the annealed sample, with no significant change in its g-value. Meanwhile, the lineshape of the broader **Sn2** line did not change significantly in the annealed sample. According to microstructure investigations (Section 3.1.5), the annealing resulted in the dispersion of a large part of the α-Sn NCs initially found in the as-received cBN crystallites. This result strongly suggests that the paramagnetic centers responsible for the **Sn1** line are associated with the presence and amount of the α-Sn NCs in the cBN crystallites, while the **Sn2** line does not seem to be related to the presence of α-Sn NCs. Therefore, the **Sn2** component ESR line was not further investigated. However, one should mention that the temperature evolution of this line, which remains unchanged after annealing, corresponds to a paramagnetic system of certain point defects. Based on the observed effective g-values, they could be associated with Sn^{3+}

Figure 8. Temperature-induced variation of the Q-band **Sn1** line parameters: (a) amplitude A_1 and (b) integrated intensity $I_1 = A_1 \times (\Delta B_1)^2$. The experimental data (dots) are fitted with functions (solid red lines) involving the QC-induced discrete conduction electron energy levels with Δ_i spacing, as described in Sections 3.3.3 and 3.3.4. The fitting functions are given in Table 4, lines 2 and 3.

ions localized at cBN lattice sites. This is a subject that remains to be investigated.

The narrow, symmetrical Lorentzian **Sn1** line, with no resolved structure observed in the dark cBN crystallites, can be described by a simple spin Hamiltonian consisting of only the Zeeman interaction, with usual notations:[47]

$$H = \mu_B S \cdot g \cdot B \tag{1}$$

Here, $S = 1/2$ and $g = 2.0028 \pm 0.0001$. Additional information about the nature of the paramagnetic centers responsible for the **Sn1** line is provided by the analysis of its properties (g-value, linewidth, and integrated intensity) as a function of the measuring temperature. The ESR parameters of the **Sn1** line were determined from the analysis of the spectra recorded at low enough microwave power P_{mW} levels to avoid saturation effects, as determined from the $I_1 vs (P_{mW})^{1/2}$ variation at RT, 100 K, 70 K, and 30 K (see Figure S6a−d in the Supporting Information) and with a modulation amplitude of 0.06 mT. The fitting/deconvolution of the ESR spectra is detailed in the Supporting Information, with deconvolution examples in Figure S7 for the spectra measured in both X- and Q-bands at different temperatures.

As previously mentioned, the g-value is temperature- and microwave frequency-independent, with a very small g-shift ($\Delta g = g - g_e = 0.0005$) from the free electron $g_e = 2.0023$ value (Figure 7a,b).

Meanwhile, its derivative peak-to-peak linewidth, denoted as ΔB_1, exhibits a specific temperature dependence, better observed in the Q-band ESR spectra, recorded over a broader temperature range (Figure 7b). Thus, the ΔB_1 linewidth exhibits for $T < 125$ K a sharp drop with temperature decrease, from 0.19 mT at $T = 125$ K to 0.08 mT at $T = 20$ K, while for $T > 125$ K, the ΔB_1 value slightly decreases with temperature increase from 0.19 mT at $T = 125$ K to 0.18 mT at 295 K. A similar higher temperature dependence, namely, a decrease in ΔB_1 with temperature increase from 0.18 mT at $T = 100$ K to 0.15 mT at $T = 295$ K, is observed in the X-band (Figure 7a).

Comparing the ESR spectra of the as-received and vacuum-annealed cBN samples recorded at RT (see Figure S5a,b in the Supporting Information), one observes a strong drop in the amplitude A_1 of the **Sn1** line in the annealed cBN. A small increase in its ΔB_1 linewidth value, from 0.15/0.18 mT in the as-received cBN to 0.20/0.38 mT in the vacuum-annealed cBN, for both X/Q frequency bands, respectively, was also observed. The temperature dependences of the amplitude A_1 and integral intensity I_1 of the Lorentzian **Sn1** line, calculated

as the product of the line amplitude and peak-to-peak linewidth squared:[51,52]

$$I_1 = A_1 \times (\Delta B_1)^2 \tag{2}$$

have been determined for the as-received cBN crystallites from the Q-band ESR spectra (Figure 8a,b), where the influence of the partly overlapping broad **Sn2** line was less pronounced.

One should mention that reliable ESR data could not be obtained for $T < 20$ K because of a strong increase in the microwave absorption, attributed to an increase in the electrical conductivity of the α-Sn NCs. This effect, hampering the tuning of the ESR spectrometer microwave bridge, suggests the proximity of a superconductive transition at $T < 20$ K. To our knowledge, such an enhancement of the electrical conductivity and occurrence of collective magnetism by nanosizing, previously observed at $T = 3.98$ K for β-Sn NPs with $d = 10$ nm,[53,54] has not been reported in α-Sn NCs. A similar temperature dependence as in Figure 8b has been reported[55] for the magnetic susceptibility of magnesium nanoparticles with 1.4 and 1.7 nm diameters. The observed drop in susceptibility toward the lowest temperatures from a maximum value at $T \sim 40$ K has been attributed to QC, while the slow decrease in the susceptibility with temperature increase for $T > 50$ K could not be explained.

3.3. Properties of the Sn1 ESR Line and Resulting Data Analysis. *3.3.1. The Origin of the Sn1 Line: The CESR of the α-Sn NCs.* According to the present a-(HR)STEM/TEM and ESR investigations, the observed drop in the amplitude/intensity of the **Sn1** ESR line in the cBN crystallites vacuum-annealed at 950 °C is accompanied by the thermally activated diffusion and further oxidation of the Sn atoms at the surface of the host cBN crystallites. It is very likely that the diffusing Sn atoms are at least partly provided by the dissolution of the α-Sn NCs incorporated in the cBN crystallites. This explains the absence of α-Sn NCs in the STEM image (Figure 5) of the annealed cBN samples. Thus, it seems very likely that the narrow, intense Lorentzian-shaped **Sn1** component ESR line observed in the as-received cBN crystallites originates in the α-Sn NCs, while the low intensity **Sn1** line with identical $g = 2.0028$ factor, observed in the ESR spectra of the annealed cBN crystallites, could originate in the remaining, partly dissolved α-Sn NCs, which are too small to be observed in the STEM images in the observational magnification range. The observed symmetrical Lorentzian line (see Figure 7 in the Supporting Information), instead of an asymmetrical Dysonian shape typical for bulk CESR lines, is

explained by the nanometer size of the α-Sn NCs, much smaller than the micrometer skin depth of the X/Q-band microwaves.[49,50]

As will be demonstrated here, the observed **Sn1** linewidth ΔB_1 and line intensity I_1 temperature dependences can be also explained by the CESR properties of the α-Sn NCs identified in the as-received and annealed cBN crystallites. The CESR origin of the **Sn1** line in the α-Sn NCs with metallic character is supported by the independence of its $g = 2.0028$ value on both temperature and microwave frequency and its very small g-shift. Moreover, we will show that the assignment of the **Sn1** line to the CESR of the α-Sn NCs is essential in obtaining a good quantitative fit of the observed **Sn1** linewidth and line intensity *vs* temperature variations.

3.3.2. Evidence of Quantum Confinement from the Sn1 Linewidth vs Temperature Variation. The strong decrease in **Sn1** linewidth with temperature decrease below $T \sim 125$ K (Figure 7b) can be explained in a semiquantitative manner by correlating the known electron energy quantization properties of the small metallic particles with the observed microstructure and morphology properties of the α-Sn NCs. Indeed, when the size of the metallic particles diminishes to a certain critical value, which depends on the nature of the investigated material, QC is expected to occur,[37,56] i.e., the allowed electronic states should be chosen from a restricted basis set that incorporates the boundary conditions.[38–40,50] In this case, the CESR linewidth is expected to sharply decrease with further nanoparticle (NP) size decrease. Such an effect was reported for the ESR spectra of metallic Li NPs with average size from 300 to 10 nm,[57] which exhibited a symmetrical, Lorentzian CESR line with constant $g = 2.002$ value and a sharp linewidth decrease from 0.82 mT for NPs of 100 nm diameter to 0.19 mT for NPs of 10 nm diameter. In a later ESR investigation of metallic Li NPs with $d_m = 3.2$ nm average diameter, it was reported[58] that at lower temperatures ($T < 20$ K), the intensity of the CESR line changed from a classical Pauli-type temperature-independent value at higher temperatures to a Curie-type temperature dependence attributed to the QC effect.

The characteristics of the **Sn1** line attributed to the α-Sn NCs observed in the dark cBN crystallites are in certain aspects similar to those of the small metallic Li NPs, namely, a constant g-value and a sharp decrease in ΔB_1 with temperature decrease from 0.19 mT at $T = 100$ K to 0.08 mT at $T = 20$ K. One also notices the decrease in **Sn1** linewidth ΔB_1 with temperature increase at $T > 125$ K (Figure 7b), a feature that will be discussed in the next section.

First, we shall demonstrate, in a semiquantitative manner, how the strong narrowing of the **Sn1** linewidth ΔB_1 with temperature decrease observed at lower temperatures ($T < 125$ K) (Figure 7b) reflects the presence of QC. It is known[38,40] that such a narrowing of the CESR line of nanosized metal particles occurs if the following conditions are accomplished:

$$\hbar\omega_s/\delta \ll 1 \text{ (a)}, \quad \hbar/\tau\delta \ll 1 \text{ (b)}, \quad |\Delta g| \ll 1 \text{ (c)} \tag{3}$$

Once the conditions (eq 3) are satisfied, the linewidth can be expressed as:

$$\Delta B \sim \hbar\omega_s/\tau\delta \tag{4}$$

Here, $\hbar\omega_s$ is the observed microwave energy, and $\tau \sim d/V_F\Delta g^2$ is the spin–lattice relaxation time, where d is the linear dimension of the particles, while $V_F = 1.90 \times 10^6$ m/s and $E_F = 10.2$ eV are the Fermi velocity and energy values for Sn,

respectively.[59] $\Delta g = g - g_e$ is the g-shift and $\delta = 4E_F/3N_e$ is the inverse of the average density of electronic states for a single spin at the Fermi energy E_F, with N_e being the number of electrons per nanoparticle. For quasi-spherical NPs, as in our case, the QC-induced discrete electron energy level spacing δ is given by the relation:

$$\delta = Cd^{-3} \tag{5}$$

Here, C is a constant, which can be obtained for several types of metal colloidal particles from the $\delta/k_B \, vs \, d$ graphical dependences presented in Figure 1 of ref 39. As previously mentioned, the TEM examination of a cBN sample revealed a log-normal distribution of 79 small α-Sn NCs (Figure 4b) with an average diameter $d_m = 2.5$ nm. This value corresponds[39] to a QC-induced energy level spacing $\delta/k_B = (100 \pm 20)$ K, suggesting the onset of QC-induced line narrowing at $T \sim 100$ K, in agreement with our observations (Figure 7b). One also notices that the inequality (3a) is fulfilled even for the higher Q-band frequency (34.125 GHz), i.e., $\hbar\omega_s/k_B = 1.63$ K $\ll \delta/k_B = 100$ K. The calculation of the spin–lattice relaxation time, using the values $d = 2.5$ nm, $V_F = 1.90 \times 10^6$ m/s, and $|\Delta g| = 0.0005$, gives $\tau \sim d/V_F\Delta g^2 = 5.26 \times 10^{-9}$ s. Considering that $\delta/k_B \sim 100$ K, one obtains $\tau\delta = 3.81 \times 10^{-29}$ J s $\gg \hbar = 1.055 \times 10^{-34}$ J s, which confirms the validity of condition (3b). The inequality (3c) is also valid for the observed $|\Delta g| = 0.0005$ value.

According to Kubo et al.,[38,40] the sharp decrease in ΔB_1 with temperature decrease, observed here for $T < 125$ K (Figure 7b), is attributed to the QC of the conduction electron orbital motion in the α-Sn NCs. However, the whole observed $\Delta B_1(T)$ variation (Figure 7b) cannot be accurately described by a reciprocal temperature dependence or a simple temperature-independent term.[40] To explain the observed $\Delta B_1 \, vs$ temperature variation of the **Sn1** line, we will first consider the energy loss of the unpaired electrons by relaxation from the microwave pumped spin excited state, a process characterized by the longitudinal T_1 and transversal T_2 relaxation times. One notices that for metals $T_1 = T_2$, as the spin–spin interaction is relatively weak and the velocity of the conduction electrons on the Fermi surface is high.[38] Hence, the CESR linewidth directly measures the spin–lattice relaxation rate $\Delta B_1 \sim 1/T_1$, which for simple metals is usually linear in temperature, probing the electron density of states at the Fermi level $N(E_F)$ according to the Korringa law:[60]

$$\Delta B = b \times T, \text{ where } b \sim N^2(E_F) \tag{6}$$

For a Lorentzian ESR line, the relaxation time T_1 is related to the derivative peak-to-peak linewidth ΔB_1 through the general relation:

$$T_1 = 2/(3)^{1/2}[\gamma_e(\Delta B_1)]^{-1} \tag{7}$$

Here, $\gamma_e = eg_e/2m_e = 1.760859 \times 10^{11}$ s^{-1} T^{-1} is the electron gyromagnetic ratio.[61]

Contributions to the spin–lattice relaxation process are usually expected from electron scattering by lattice vibrations, collision with lattice defects (including impurities), and α-Sn NC surface scattering. These processes, usually characterized by corresponding T_{sl}, T_r, and T_s relaxation times, provide additive contributions to the relaxation rate: $1/T_1 = 1/T_{sl} + 1/T_r + 1/T_s$. In the presently investigated small α-Sn NCs with low content of impurities and lattice defects, one expects the scattering on the surface to be dominant,[57] i.e., $T_s \approx T_1$.

Using eq 7 and the experimental $\Delta B_1 vs\ T$ variation (Figure 7b), the resulting $1/T_1 vs\ T$ dependence given in the inset of Figure 9 can be approximated at lower temperatures ($T < 60$
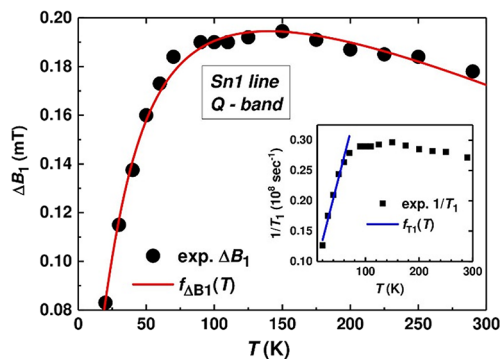
Figure 9. Temperature dependence of the ΔB_1 linewidth (dots) and its fitting function (solid red line) reflecting a direct relaxation process (inset) and a thermally activated process involving an excited state at $\Delta_{up}/k_B = 120$ K above the magnetic doublet level responsible for the **Sn1** line. The fitting function is given in Table 4, line 1. Inset: temperature dependence of the relaxation rate $1/T_1$ determined with eq 7 and the experimental $\Delta B_1 vs\ T$ data. The linear temperature dependence $f_{T_1}(T)$ (solid blue line), which fits the $1/T_1$ data (squares) only at $T < 60$ K, evidences the presence of QC.

K) by a linear temperature dependence $f_{T_1}(T)$: $1/T_1$ (10^8 s^{-1}) $= 0.0666 + 0.0034T$ (Figure 9, inset), reflecting a dominant direct relaxation mechanism.[40] Indeed, one finds that the previously calculated $\tau \sim d/V_F\Delta g^2 = 5.26 \times 10^{-9}$ s value is comparable, considering all approximations involved, with the spin−lattice relaxation time $T_1 \sim 4.8 \times 10^{-8}$ s at $T = 50$ K obtained with the relaxation rate in Figure 9 (inset).

*3.3.3. The QC-Induced Discrete Conduction Electron Energy Level Separation Determined from the Observed $\Delta B_1 vs$ Temperature Dependence of the **Sn1** Linewidth.* The experimental $\Delta B_1 vs\ T$ dependence of the **Sn1** line in the whole investigated temperature range (Figure 7b) can be accurately described with the following formula:[62]

$$\Delta B_1 = \Delta B_0 + bT + c/[\exp(\Delta_{up}/k_BT) - 1] \qquad (8)$$

Here, ΔB_1 is the derivative peak-to-peak linewidth (in mT) measured at temperature T, and ΔB_0 is the residual linewidth, presumably accounting for the spin−spin interactions and inhomogeneous broadening, which for the present α-Sn NCs are vanishingly small. The factor $b = 4.25 \times 10^{-3}$ mT/K (see Table 4) is similar to the Korringa b parameter from eq 6, which describes the direct single-phonon relaxation process dominant at low temperatures. The last term in eq 8 usually describes the relaxation via an excited state situated at Δ_{up} above the magnetic doublet level responsible for the **Sn1** line.[62,63] This contribution is due to the modulation of the ligand field by lattice vibrations through the spin−orbit coupling, giving rise to a spin−lattice relaxation involving vibrational states situated above the ground state.[40,63]

In our case, the last term in eq 8 brings a negative thermally activated contribution, associated with the presence of a negative relaxation rate ($c < 0$), which would be difficult to explain. However, its line narrowing effect at $T > 150$ K could be explained by the presence of a fast dynamical process, compensating for the line broadening effect of the second term in eq 8. Thus, the third term in eq 8 could be an empirical

Table 4. Fitting Parameters for the Observed Temperature Dependence of the Linewidth ΔB_1, Amplitude A_1, and Intensity I_1 of the Sn1 Line from the α-Sn NCs in the As-Received (First Three Lines) and Vacuum-Annealed (Fourth Line) Dark cBN Crystallites Obtained with eqs 8, 10, and 11, Respectively[a]

no.	fitting functions/figure with experimental data	ΔB_0 (mT)	b (10^{-3} mT/K)	c (mT)	Δ_i/k_B i = up, low, QC (K)[b]	A_0 (10^5 arb. units)	a (arb. units)
1	$f_{\Delta B1}(T) = \Delta B_0 + bT + c/[\exp(\Delta_{up}/k_BT) - 1]$ (Figure 9)	0 ± 0.01	4.2 ± 0.1	-0.54 ± 0.02	120 ± 14		
2	$f_{A1}(T) = A_0/[1 + a\exp(\Delta_{low}/k_BT)]$ (Figure 8a)				130 ± 20	9.3 ± 2.4	0.8 ± 0.4
3	$f_{I1}(T) = \{A_0/[1 + a\exp(\Delta_{QC}/k_BT)]\}\{\Delta B_0 + bT + c/[\exp(\Delta_{QC}/k_BT) - 1]\}^2$ (Figure 8b)	0	4.2 ± 0.3	-0.54 ± 0.3	125 ± 20	7.7 ± 3.0	0.7 ± 0.5
4	$f_{\Delta B1}*(T) = \Delta B_0 + bT + c/[\exp(\Delta_{up}*/k_BT) - 1]$ (Figure 10)	0.07 ± 0.01	1.5 ± 0.1	-20 ± 15	1500 ± 600		

[a]Superscript asterisks (*) indicate cBN crystallites vacuum-annealed for 4 h at 950 °C. [b]Some helpful energy unit conversions: 125 K ↔ 10.8 meV; 1500 K ↔ 129.3 meV.
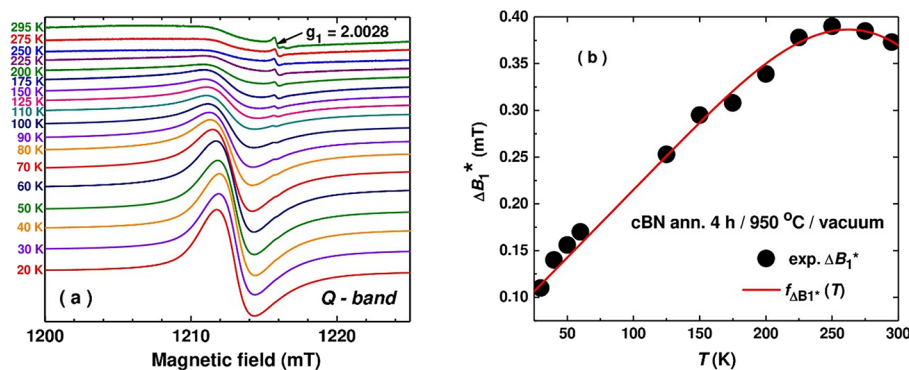
Figure 10. (a) ESR spectra of the dark cBN crystallites vacuum-annealed for 4 h at 950 °C, recorded in the Q-band (34.08 GHz), from 20 to 295 K. (b) Resulting temperature variation of the linewidth ΔB_1^* of the remaining **Sn1** line (dots) fitted with eq 8 (solid red line). The fitting function is given in Table 4, line 4.

description of a thermally activated dynamical line narrowing process involving an excited state.

3.3.4. Evidence of QC-Induced Conduction Electron Discrete Energy Levels in the Temperature Variation of the Sn1 Line Intensity I_1. As can be seen in Figure 8a, the variation of the **Sn1** CESR line amplitude A_1 with temperature is well fitted with the formula:

$$A_1 = A_0/[1 + a \exp(\Delta_{\mathrm{low}}/k_{\mathrm{B}}T)] \qquad (9)$$

where the parameters A_0 and a are given in arbitrary units in Table 4 and $\Delta_{\mathrm{low}}/k_{\mathrm{B}} = 130$ K.

While the width of the **Sn1** line is determined by the spin–lattice interaction, its amplitude A_1 and intensity I_1 are expected to reflect the number of conduction electrons involved in the microwave absorption process. Thus, for weakly interacting electrons, i.e., neglecting the spin–spin interactions, the intensity of an ESR signal can be written as:[47,48]

$$I_1 \sim n = n_2 - n_1 \sim N\hbar\omega/2k_{\mathrm{B}}T \qquad (10)$$

Here, n is the difference in the population of the electrons in the Zeeman doublet levels $S = 1/2$, $M_S = \pm 1/2$, while $N = n_2 + n_1$ is the total number of electrons involved in the ESR process. According to eq 10, for a constant N value, one expects a Curie-type behavior, with I_1 decreasing with temperature increase, unlike the observed temperature dependence (Figure 8b). One of the factors contributing to this behavior, previously observed for certain localized paramagnetic centers in semiconductors, is an increase in the N population of electrons responsible for the ESR spectrum due to the thermal excitation of the electrons from a lower donor energy level.[41,65] $\Delta_{\mathrm{low}}/k_{\mathrm{B}}$ from eq 9 is, therefore, the energy separation between the lower donor level, source of the thermally excited electrons, and the CESR magnetic doublet level responsible for the **Sn1** line.

Based on the successful fitting of the experimental temperature dependence of the ΔB_1 linewidth (Figure 9) and line amplitude A_1 (Figure 8a) with eqs 8 and 9, respectively, one obtains an excellent fit of the temperature dependence for the integrated intensity I_1 of the **Sn1** line (Figure 8b) with the formula:

$$I_1 = A_1 \times (\Delta B_1)^2$$
$$= \{A_0/[1 + a \exp(\Delta_{\mathrm{QC}}/k_{\mathrm{B}}T)]\}$$
$$\{\Delta B_0 + bT + c/[\exp(\Delta_{\mathrm{QC}}/k_{\mathrm{B}}T) - 1]\}^2 \qquad (11)$$

Here, we used the same notations as those employed in eqs 8 and 9, excepting the energy separations between the magnetic $S = 1/2$ doublet level responsible for the **Sn1** line and the neighboring lower and upper levels, replaced here by the Δ_{QC} average separation. The fitting parameters given in Table 4 (line 3) exhibit values close to those obtained from the separate fitting of the temperature dependences of ΔB_1 (Table 4, line 1) and amplitude A_1 (Table 4, line 2), which confirms the validity of the above analysis. We should mention that our attempts to fit the intensity I with eq 9 resulted in a $\Delta_{\mathrm{low}}/k_{\mathrm{B}} = 218$ K value and did not match satisfactorily the experimental data in the 175–290 K region. Including supplementary energy level terms in the fitting of eq 9 did not improve the fitting either, a result that excludes the presence of other neighboring donor or acceptor levels.

Comparing the fitting parameters from Table 4, lines 1 to 3, one notices the close values, within the experimental errors, of the $\Delta_{\mathrm{up}}/k_{\mathrm{B}}$ and $\Delta_{\mathrm{low}}/k_{\mathrm{B}}$ energy level separations of the magnetic doublet level, source of the **Sn1** line, from the upper energy level involved in the relaxation process, on the one hand, and from the lower energy level, source of the thermally excited conduction electrons, on the other hand. Another remarkable aspect is that the average $\Delta_{\mathrm{QC}}/k_{\mathrm{B}} = 125$ K energy separation between the identified energy levels, obtained from fitting the $I_1 vs T$ dependence, compares well, within the experimental errors (± 20 K) involved, with the $\delta/k_{\mathrm{B}} \sim 100$ K value of the QC-induced conduction electron energy level spacing, determined with eq 5[38,40] for the α-Sn NCs of 2.5 nm average diameter found in the cBN crystallites.

The equivalence between the QC-induced conduction electron energy level spacing resulting from fitting the temperature variation of ΔB_1 and A_1 (or I_1) and the δ/k_{B} energy level separation obtained for the α-Sn NCs of 2.5 nm diameter is further confirmed by the analysis of the temperature dependence of the ΔB_1^* linewidth of the weak **Sn1** line observed in the annealed cBN crystallites. This line, with the same constant $g = 2.0028$ factor, is attributed to the remaining α-Sn NCs with diameters $d < 1.3$ nm, a size too small to be directly observed in the STEM images obtained at a higher magnification. The Q-band ESR spectra of the vacuum-annealed dark cBN crystallites, recorded between 20 and 295

K with a higher sensitivity compared to the spectra of the as-received sample (Figure 6b), are displayed in Figure 10a.

As shown in Figure 10b, the resulting ΔB_1^* vs temperature dependence is well fitted with eq 8 and the parameters given in Table 4, line 4. One notices the larger margin of errors due to a less accurate separation by numerical deconvolution—simulation of the low intensity **Sn1** line from the more intense **Sn2** line. The rather large $\Delta_{up}^*/k_B = (1500 \pm 600)$ K fitting value of the QC-induced discrete conduction electron energy level separation leads, according to eq 5, to an average diameter $d_a = 1.014$ nm for the α-Sn NCs in the annealed host crystals, a value that explains their unobservability in the STEM images. According to the same Table 4 values, the larger low temperature linewidth of the **S1** line in the annealed sample compared to the linewidth of the as-received sample is due to the residual linewidth contribution ($a = 0.07$ mT), which reflects an inhomogeneous broadening originating in the increased surface-induced disorder in the very small α-Sn NCs remained after annealing.

4. DISCUSSION

The a-(HR)STEM/TEM investigations revealed nanosized aggregates of Sn impurity atoms, as quasi-spherical NCs with an undistorted diamond cubic α-Sn single phase structure, incorporated in dark cBN crystallites. According to the ADF-STEM and (HR)TEM images, the dimensions of these α-Sn NCs belong mainly to two size classes, small ones (<5 nm), which prevail, and a few large (>20 nm) ones. For example, we found in a TEM image at high magnification (Figure 4a) the presence, besides two large α-Sn NCs of 22.5 and 37 nm, of a distribution of 79 smaller α-Sn NCs ranging from 1.4 to 5.4 nm in size, with average diameter $d_m = 2.5$ nm. The HRTEM examination of the largest quasi-spherical α-Sn NC of 37 nm diameter revealed an undistorted, high quality α-Sn crystalline lattice, with a low density of defects, reflecting a good accommodation within the cBN host lattice, despite the large difference in the lattice parameters of α-Sn ($a_0 = 0.6489$ nm) and cBN ($a_0 = 0.36157$ nm). Because the smaller α-Sn NCs exhibit a better stability in the diamond cubic structure,[32] one expects the same high crystalline quality for the small α-Sn NCs as for the large ones.

The stabilization in the cBN lattice of the cubic α-Sn NCs above $T_c = 13.2$ °C, the bulk α-β phase transition temperature, previously reported for the Si and Ge host lattices with similar structures, is explained by the interplay between interface and pressure effects.[30,32] This is confirmed by our HRTEM images, which reveal clear interfaces, with no separating layer between the α-Sn NCs and the cBN host lattice. Moreover, the quasi-spherical shape of the α-Sn NCs minimizes the surface area and, therefore, the interfacial energy between the NCs and the cBN host lattice, as in the case of α-Sn NCs in Ge.[32]

One concludes that the formation and growth of the α-Sn NCs during the HP-HT synthesis process of the cBN crystallites are based on a diffusion-assisted, phase separation mechanism. We found this process to be reversed by annealing the cBN host crystallites at 950 °C in vacuum ($P < 10^{-4}$ mbar), resulting in the dissolution of the α-Sn NCs, with ejection and oxidation of the Sn atoms and formation of nanocrystalline SnO_2. Moreover, because α-Sn NCs could not be observed in the STEM images of the annealed cBN crystallites, even at higher magnifications, but are evidenced by their **Sn1** CESR line, one concludes that a fraction of the α-Sn NCs with very small diameters ($d < 1.3$ nm), resulting from the

partial dissolution of the larger α-Sn NCs, are still left in the cBN host lattice.

Valuable information about the conduction electron properties in the α-Sn NCs embedded in the dark cBN crystallites has been obtained by examination of the symmetrical, narrow Lorentzian-shaped **Sn1** line properties in the 20 to 295 K temperature range. Thus, the independence of its $g = 2.0028$ value on temperature in both X- and Q-band frequencies and its small g-shift are attributed to the CESR of the α-Sn NCs with metallic character and 2.5 nm average diameter by demonstrating that conditions (3a), (3b), and (3c) for the QC of conduction electrons in small metallic colloids[38,40] are accomplished by the **Sn1** line as well.

A semiquantitative analysis of the Q-band ΔB_1 vs temperature dependence (Figure 7b) confirms the CESR origin of the **Sn1** line, reflected in the QC-induced linewidth narrowing below 125 K, a value close to the QC-induced energy level spacing $\delta/k_B = 100$ K calculated with eq 5 for the α-Sn NCs of 2.5 nm average size.[38,40]

Further, a good fitting of the whole recorded temperature-induced dependences of the **Sn1** linewidth ΔB_1 (Figure 9) and line intensity I_1 (Figure 8b) has been obtained by including additional exponential terms (Table 4) in eqs 8, 10, and 11. These terms reflect a QC-induced fine structure in the energy spectrum of the conduction electrons consisting of distinct levels at Δ_{up}/k_B above and Δ_{low}/k_B below the $S = 1/2$ magnetic doublet level source of the **Sn1** line. The average $\Delta_{QC}/k_B = 125$ K ± 20 K energy level separation is in good agreement with the calculated QC-induced energy level spacing value $\delta/k_B = 100$ K determined according to the theory of small metallic colloids.[38,40] To our knowledge, the presence of such QC-induced discrete conduction electron energy levels has not been evidenced experimentally in conductive nanoparticles, at least from ESR investigations.

The specific **Sn1** line properties, namely, the very small and frequency-independent g-shift ($\Delta g = 0.0005$), suggesting an almost pure s-type conduction electron ground state, as well as the presence of discrete conduction electron energy levels with Δ_{QC}/k_B average separation, can tentatively be explained based on the theoretically predicted electron quantum properties of small, unstrained α-Sn NCs, in comparison with the bulk α-Sn electron properties. Thus, according to first-principles calculations,[19,20,23] the unstrained bulk α-Sn electron properties are due to an electron energy band ordering built from Sn $5s_{1/2}$ and Sn $5p_{3/2}$ atom orbitals, with the 4-fold degenerated light-hole valence p-like Γ_{8v} band pinned to the bulk Fermi energy (E^b_F), while the usually conductive s-like Γ_{6c} states could move up and down in energy. Considering the strong spin–orbit coupling (SOC) as well, the α-Sn bulk band ordering $\Gamma_{7v} < \Gamma_{6c} < \Gamma_{8v}$, schematically drawn in Figure 11a, was reported.[23] Here, the zero gap properties of the bulk α-Sn result[19,66] from the degenerate states at the Γ point, where the heavy-hole valence band and the electron conduction band touch each other at Γ_{8v}.

Additional information about the nanosizing influence on the electron energy properties of α-Sn NCs in cBN can be obtained by comparing the presently reported ESR data with the published results of *ab initio* first-principles calculations performed for supercells containing from 5 up to 525 Sn atoms, i.e., corresponding to α-Sn NCs with diameters from 0.4 to 4 nm.[23] Thus, the calculated electron energy band positions (Figure 11b) evidence the opening of a band-gap Δ_G separating the lower-valence HOMO (highest occupied
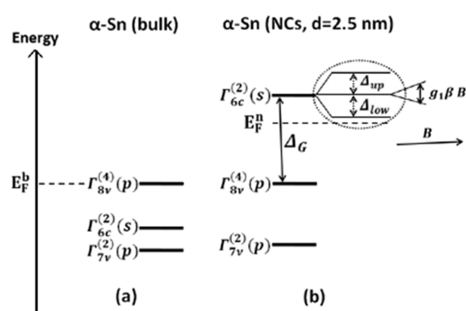
Figure 11. Suggested energy band structure along the Γ direction in the reciprocal space for (a) bulk α-Sn[19,23] and (b) small α-Sn NC according to refs 22 and 23 and to the present ESR data. The upper indices denote the spin degeneracy order of the respective states. Part of the energy level fine structure of the conductive Γ_{6c} band, attributed to QC of the conduction electron orbital motion in the α-Sn NCs,[38,40] with its $\Delta_i/k_B \sim 120$ K spacing, is presented in an expanded view (dashed circle) on the top right side of the diagram. The suggested position of the Fermi energy level E_F^n with respect to the lowest energy level of the Γ_{6c} band fine structure, estimated from the thermally activated properties of the **Sn1** line, is also presented.

molecular orbital) state centered on the Γ_{8v} level from the upper-conductive LUMO (lowest unoccupied molecular orbital) state centered on the Γ_{6c} level. The band-gap formation results from the lifting of the conductive s-like Γ_{6c} level above the p-like Γ_{8v} level, which fixes the top of the valence band in the Γ point of the Brillouin zone (BZ). It has been also found that the lifting of the Γ_{6c} band leads to the QC-induced energy band inversion of the α-Sn NCs state order $\Gamma_{7v} < \Gamma_{8v} < \Gamma_{6c}$ with respect to the bulk α-Sn state order $\Gamma_{7v} < \Gamma_{6c} < \Gamma_{8v}$, i.e., to a topological transition, estimated[23] to occur for α-Sn NCs of $d \sim 12$ nm. The absence of such transition for the two large α-Sn NCs with diameters of 22.5 and 37.35 nm, observed by TEM, could explain the absence of any associated CESR line in the ESR spectrum. Using the data from Figures 4 and 6 of ref 23, one also obtains for the α-Sn NCs with $d_m = 2.5$ nm (239 Sn atoms) a $\Delta_G = 1.03$ eV value, comparable to the $\Delta_G = 1.17$ eV value based on data from Table 2 of ref 36.

According to the energy levels and angular momentum-resolved density of states calculations,[23] the upper LUMO level of the conduction band is formed mainly from bulk Sn 5s states of the Γ_{6c} level, while the lower HOMO level in the valence band is formed mainly from the bulk Sn 4p states of the Γ_{8v} level. The calculated dominant Sn 5s-like Γ_{6c} orbital contribution in the above-the-gap level in the conduction band explains the observed s-type character of the resonant $S = 1/2$ magnetic doublet level responsible for the **Sn1** line.

The presence of the two conduction electron levels, with similar $\Delta_i/k_B \sim 125$ K separations below and above the $\Gamma_{6c}S = 1/2$ magnetic doublet level responsible for the **Sn1** ESR line, as illustrated in the enlarged upper part of Figure 11b, suggests a Fermi level position close to the Γ_{6c} state of the LUMO level. This could explain the ESR observed thermally activated population of the LUMO states with unpaired s-electrons, as well as the conductive metal-like properties of the α-Sn NCs. The similar, small separation of the two levels from the ground magnetic doublet ($\sim$10 meV in the as-received samples), orders of magnitude smaller than the separation of the conduction electron energy levels shown in Figure 11, built from Sn atomic states, suggests the harmonic confining

potential in small nanoparticles[64] as a possible origin of these energy levels.

To complete our discussion, we shall examine the possibility of alternative sources for the **Sn1** line in the investigated cBN crystallites. One possibility would be some paramagnetic point defect, which happens to be thermally bleached during the vacuum annealing of the cBN crystallites, such as atomic/impurity-type defects localized in the cBN lattice or in the α-Sn NCs. In both cases, one expects broader Gaussian-shaped lines due to the unresolved hyperfine structures from the interaction of the unpaired $S = 1/2$ electron spin with the nuclear spins $I = 3/2$ of the [11]B isotopes (81.17% nat. abund.) and $I = 1$ of the ^{14}N isotopes (99.635% nat. abund.), in the cBN host, or from the interaction of the unpaired $S = 1/2$ electron spin with the nuclear spin $I = 1/2$ of the two odd isotopes [117]Sn and [119]Sn with natural abundance values of 7.6 and 8.6%, respectively, in the case of the α-Sn host.

The presence of a thicker Sn-oxidic surface layer[27] hosting the paramagnetic defects is also excluded, as the HRTEM images reveal sharp α-Sn NCs−cBN interfaces. Moreover, in the case of paramagnetic point defects incorporated in wide band-gap oxidic or cBN hosts, one expects the temperature variation of the **Sn1** line intensity to obey a Curie-type law in the whole temperature range,[39,50] different from the presently observed $I_1 vs T$ variation (Figure 8b), reflecting QC effects.

One should also mention that $S = 1/2$ paramagnetic species with g-factor and linewidth values close to those of the presently investigated **Sn1** center have been reported in materials containing carbon clusters.[67,68] However, in the absence of any reported linewidth and/or line intensity vs temperature data evidencing QC effects, the reported g-factor and linewidth values similar to those of the **Sn1** center could be a simple coincidence. Moreover, our a-(HR)STEM/TEM observations did not evidence any carbon aggregates in the dark cBN crystallites.

5. CONCLUSIONS

Correlated analytical (HR)STEM/TEM and multifrequency ESR investigations of HP-HT-grown dark cBN crystallites from a batch of large-grained, BORAZON CBN Type 1, 60/70 FEPA B251 superabrasive powder resulted in the following major findings:

The Sn impurity atoms incorporated in the cBN crystallites during the HT-HP synthesis did aggregate in quasi-spherical NCs with undistorted diamond cubic α-Sn single phase structure, predominantly of small average 2.5 nm diameter and a few larger ones.

The stabilization in the cBN lattice of the cubic α-Sn NCs above the $T_c = 13.2$ °C bulk α-β transition temperature, previously reported for the Si and Ge host lattices of similar structure and explained by the interplay between interface and pressure effects, is supported by the present HRTEM images, which revealed clear interfaces with no separating layer.

The investigation of the cBN crystallites submitted to thermal annealing confirmed the presence of a diffusion-assisted phase separation mechanism involved in the formation and growth of the α-Sn NCs during the HP-HT synthesis of the host cBN crystallites, probably with Sn as a catalyst. This process could be reversed by vacuum annealing at 950 °C, with the partial dissolution of the α-Sn NCs and the ejection and oxidation of the resulting Sn atoms.

The symmetrical, narrow Lorentzian-shaped **Sn1** line observed in the ESR spectrum was attributed to the CESR

of the small α-Sn NCs with metal-like properties, in agreement with its temperature- and microwave (X- and Q-band) frequency-independent $g = 2.0028$ factor, its very small $\Delta g = 0.0005$ shift, and the particular temperature dependence of the Q-band ΔB_1 linewidth and I_1 line intensity in the investigated 20 to 295 K temperature range.

Thus, the analysis of the low temperature $\Delta B_1 vs T$ variation of the **Sn1** line (Figure 7b) demonstrated that the specific conditions for the QC of conduction electrons in small metallic colloids[38,40] are accomplished at $T < 125$ K for the small ($d_m = 2.5$ nm) α-Sn NCs in the as-received cBN crystallites.

The small, frequency-independent g-shift of the **Sn1** line, suggesting an almost pure s-type conduction electron ground state, as well as the presence of conduction electron energy levels with an average separation $\Delta_{QC}/k_B = 125$ K above and below the magnetic doublet level responsible for the **Sn1** line, determined from the quantitative analysis of the temperature variation of the ΔB_1 linewidth and I_1 line intensity, are tentatively explained with the theoretically predicted electron quantum properties of small, unstrained α-Sn NCs.[23]

Indeed, first-principles calculations of the electronic properties of small ($d < 12$ nm) α-Sn NCs[23] demonstrated that for such α-Sn NCs, a band-gap Δ_G opens at E_F^n, with a change from the bulk $\Gamma_{7v} < \Gamma_{6c} < \Gamma_{8v}$ state order to the nano $\Gamma_{7v} < \Gamma_{8v} < \Gamma_{6c}$ order induced by lifting the Γ_{6c} state above the Γ_{8v} state. The resulting band inversion, called topological phase transition, promotes mainly the Sn 5s states above the gap in the conduction band, which explains the observed temperature- and frequency-independent, small g-shift and the metal-like character of the α-Sn QDs incorporated in the cBN crystallites.

The QC-induced conduction electron discrete energy levels of the α-Sn NCs in the cBN crystallites, consisting of two energy levels situated above and below the main magnetic doublet level responsible for the **Sn1** line, evidenced by fitting the **Sn1** linewidth and line intensity vs temperature variations, could be attributed[38,40] to a restricted set of allowed electronic states selected from a basis set that incorporates the orbital motion boundary conditions.

■ ASSOCIATED CONTENT

Ⓢ Supporting Information

The Supporting Information is available free of charge at https://pubs.acs.org/doi/10.1021/acsomega.2c03785.

> Additional morphology and structure information on the dark cBN crystalline powder; microstructural and microanalytical data on the residual white powder from the vacuum-annealed dark cBN crystallites; ESR spectra of the dark cBN crystallites vacuum-annealed for 4 h at $T = 950$ °C; Q-band microwave saturation properties of the **Sn1** ESR line; deconvolution of the X- and Q-band spectra of as-received and annealed cBN and determination of the parameters of the **Sn1** CESR line (PDF)

■ AUTHOR INFORMATION

Corresponding Author

Mariana Stefan − *National Institute of Materials Physics, 077125 Magurele, Romania;* ⓞ orcid.org/0000-0001-5272-4770; Email: mstefan@infim.ro

Authors

Sergiu V. Nistor − *National Institute of Materials Physics, 077125 Magurele, Romania; Faculty of Physics, University of Bucharest, 077125 Magurele, Romania*

Leona C. Nistor − *National Institute of Materials Physics, 077125 Magurele, Romania*

Alexandra C. Joita − *National Institute of Materials Physics, 077125 Magurele, Romania; Faculty of Physics, University of Bucharest, 077125 Magurele, Romania*

Complete contact information is available at:
https://pubs.acs.org/10.1021/acsomega.2c03785

Notes

The authors declare no competing financial interest.

■ REFERENCES

(1) Wentorf, R. H. Synthesis of the cubic form of boron nitride. *J. Chem. Phys.* **1961**, *34*, 809−812.

(2) Wentorf, R. H.; DeVries, R. C.; Bundy, F. P. Sintered superhard materials. *Nature* **1980**, *208*, 873−880.

(3) Solozhenko, V. L.; Chernyshev, V. V.; Fetisov, G. V.; Rybakov, V. B.; Petrusha, I. A. Structure analysis of the cubic boron nitride crystals. *J. Phys. Chem. Solids* **1990**, *51*, 1011−1012.

(4) Vel, L.; Demazeau, D.; Etourneau, J. Cubic boron nitride: synthesis, physicochemical properties and applications. *Mater. Sci. Eng., B* **1991**, *10*, 149−164.

(5) Rapoport, E. Cubic boron nitride − a review. *Ann. Chim.* **1985**, *10*, 607−638.

(6) Taniguchi, T.; Teraji, T.; Koizumi, S.; Watanabe, K.; Yamaoka, S. Appearance of the n-type semiconducting properties of cBN single crystals grown at high pressure. *Jpn. J. Appl. Phys.* **2002**, *41*, L109−L111.

(7) Kaneko, J. H.; Taniguchi, T.; Kawamura, S.; Satou, K.; Fujita, F.; Homma, A.; Furusaka, M. Development of a radiation detector made of cubic boron nitride polycrystal. *Nucl. Instrum. Methods Phys. Res., Sect. A* **2007**, *576*, 417−421.

(8) Taniguchi, T.; Koizumi, S.; Watanabe, K.; Sakaguchi, I.; Sekiguchi, T.; Yamaoka, S. High pressure synthesis of UV-light emitting cubic boron nitride single crystals. *Diamond Relat. Mater.* **2003**, *12*, 1098−1102.

(9) Yang, X.; Ye, Q. L. Synthesis of high-quality octahedral cBN crystals with large size using lithium metal catalyst. *J. Alloys Compd.* **2013**, *580*, 1−4.

(10) Nistor, S. V.; Stefan, M.; Ghica, D.; Goovaerts, E. Multi-frequency ESR characterization of paramagnetic point defects in semiconducting cubic BN crystals. *Appl. Magn. Reson.* **2010**, *39*, 87−101.

(11) López-Morales, G. I.; Almanakly, A.; Satapathy, S.; Proscia, N. V.; Jayakumar, H.; Khabashesku, V. N.; Ajayan, P. M.; Meriles, C. A.; Menon, V. M. Room-temperature single photon emitters in cubic boron nitride nanocrystals. *Opt. Mater. Express* **2020**, *10*, 843−849.

(12) Manfredotti, C.; Lo Giudice, A.; Paolini, C.; Vittone, E.; Fizzotti, F.; Cossio, R. Characterization of impurities in cubic boron nitride crystallites with thermoluminescence and ionoluminescence. *Phys. Stat. Sol. (a)* **2004**, *201*, 2566−2572.

(13) McBride, J. R.; Rosenthal, S. J. Real colloidal quantum dot structures revealed by high resolution analytical electron microscopy. *J. Chem. Phys.* **2019**, *151*, 160903.

(14) Hou, L.; Chen, Z.; Wang, Q.; Liu, X.; Gao, Y.; Jia, G. Raman study of color zoning cubic boron nitride single crystals. *Optik* **2018**, *156*, 542−548.

(15) Tararan, A.; di Sabatino, S.; Gatti, M.; Taniguchi, T.; Watanabe, K.; Reining, L.; Tizei, L. H. G.; Kociak, M.; Zobelli, A. Optical gap and optically active intragap defects in cubic BN. *Phys. Rev. B* **2018**, *98*, No. 094106.

(16) Nistor, L. C.; Vlaicu, A. M.; Nistor, S. V. Structure of defects in semiconductor crystalline cubic boron nitride. A microstructural and microanalytical investigation. *Radiat. Meas.* **2019**, *123*, 78−82.

(17) Nistor, S. V.; Nistor, L. C.; Joita, A. C.; Vlaicu, A. M. Presence and distribution of impurity defects in crystalline cubic boron nitride. A spectroscopic study. *Radiat. Meas.* **2019**, *123*, 21−25.

(18) Sabet, S.; Kaghazchi, P. Communication: nanosize-induced restructuring of Sn nanoparticles. *J. Chem. Phys.* **2014**, *140*, 191102.

(19) Groves, S. H.; Pidgeon, C. R.; Ewald, A.; Wagner, R. J. Interband magnetoreflection of α-Sn. *J. Phys. Chem. Solids* **1970**, *31*, 2031−2049.

(20) Brudevoll, T.; Citrin, D. S.; Cardona, M.; Christensen, N. E. Electronic structure of α-Sn and its dependence on hydrostatic strain. *Phys. Rev. B* **1993**, *48*, 8629−8635.

(21) Madarevic, I.; Thupakula, U.; Lippertz, G.; Claessens, N.; Lin, P.-C.; Bana, H.; Gonzalez, S.; Di Santo, G.; Petaccia, L.; Nair, M. N.; Pereira, L. M. C.; Van Haesendonck, C.; Van Bael, M. J. Structural and electronic properties of the pure and stable elemental 3D topological Dirac semimetal α-Sn. *APL Mater.* **2020**, *8*, No. 031114.

(22) Pedersen, T. G.; Fisker, C.; Jensen, R. V. S. Tight-binding parametrization of α-Sn quasiparticle band structure. *J. Phys. Chem. Solids* **2010**, *71*, 18−23.

(23) Küfner, S.; Furthmüller, J.; Matthes, L.; Fitzner, M.; Bechstedt, F. Structural and electronic properties of α-tin nanocrystals from first principles. *Phys. Rev. B* **2013**, *87*, No. 235307.

(24) Küfner, S.; Bechstedt, F. Topological states in α−Sn and HgTe quantum wells: A comparison of ab initio results. *Phys. Rev. B* **2015**, *91*, No. 035311.

(25) Scholz, M. R.; Rogalev, V. A.; Dudy, L.; Reis, F.; Adler, F.; Aulbach, J.; Collins-McIntyre, L. J.; Duffy, L. B.; Yang, H. F.; Chen, Y. L.; Hesjedal, T.; Liu, Z. K.; Hoesch, M.; Muff, S.; Dil, J. H.; Schäfer, J.; Claessen, R. Topological surface state of α-Sn on InSb(001) as studied by photoemission. *Phys. Rev. B* **2018**, *97*, No. 075101.

(26) Rogalev, V. A.; Rauch, T.; Scholz, M. R.; Reis, F.; Dudy, L.; Fleszar, A.; Husanu, M. A.; Strocov, V. N.; Henk, J.; Mertig, I.; Schäfer, J.; Claessen, R. Double band inversion in α-Sn: Appearance of topological surface states and the role of orbital composition. *Phys. Rev. B* **2017**, *95*, No. 161117.

(27) Huang, S.; Cho, E.-C.; Conibeer, G.; Green, M. A.; Bellet, D.; Bellet-Amalric, E.; Cheng, S. Fabrication and characterization of tin-based nanocrystals. *J. Appl. Phys.* **2007**, *102*, 114304.

(28) Ihm, J.; Cohen, M. L. Equilibrium properties and the phase transition of grey and white tin. *Phys. Rev. B* **1981**, *23*, 1576−1579.

(29) Pavone, P.; Baroni, S.; de Gironcoli, S. $\alpha - \beta$ transition in tin: A theoretical study based on density-functional perturbation theory. *Phys. Rev. B* **1998**, *57*, 10421−10423.

(30) Fyhn, M. F.; Chevallier, J.; Nylandsted Larsen, A.; Feidenhans'l, R.; Seibt, M. α-Sn and β-Sn precipitates in annealed epitaxial Si$_{0.95}$Sn$_{0.05}$. *Phys. Rev. B* **1999**, *60*, 5770−5777.

(31) Lei, Y.; Möck, P.; Topuria, T.; Browning, N. D.; Ragan, R.; Min, K. S.; Atwater, H. A. Void-mediated formation of Sn quantum dots in a Si matrix. *Appl. Phys. Lett.* **2003**, *82*, 4262−4264.

(32) Ragan, R.; Atwater, H. A. Diamond cubic Sn-rich nanocrystals: synthesis, microstructure and optical properties. *Appl. Phys. A: Mater. Sci. Process.* **2005**, *80*, 1335−1338.

(33) Oehl, N.; Hardenberg, L.; Knipper, M.; Kolny-Olesiak, J.; Parisi, J.; Plaggenborg, T. Critical size for the β- to α transformation in tine nanoparticles after lithium insertion and extraction. *CrystEngComm* **2015**, *17*, 3695−3700.

(34) Arslan, I.; Yates, T. J. V.; Browning, N. D.; Midgley, P. A. Embedded nanostructures revealed in three dimensions. *Science* **2005**, *309*, 2195−2198.

(35) Haq, A. U.; Askari, S.; McLister, A.; Rawlinson, S.; Davis, J.; Chakrabarti, S.; Svrcek, V.; Maguire, P.; Papakonstantinou, P.; Mariotti, D. Size-dependent stability of ultra-small $\alpha−/\beta$-phase tin nanocrystals synthesized by microplasma. *Nat. Commun.* **2019**, *10*, 1−8.

(36) Allan, G.; Delerue, C. Optimization of carrier multiplication for more efficient solar cells: the case of Sn quantum dots. *ACS Nano* **2011**, *5*, 7318−7323.

(37) Küfner, S.; Furthmüller, J.; Matthes, L.; Bechstedt, F. Optical absorption and emission of α-Sn nanocrystals from first principles. *Nanotechnology* **2013**, *24*, No. 405702.

(38) Kubo, R.; Kawabata, A.; Kobayashi, S. Electronic properties of small particles. *Annu. Rev. Mater. Sci.* **1984**, *14*, 49−66.

(39) Halperin, W. P. Quantum size effects in metal particles. *Rev. Mod. Phys.* **1986**, *58*, 533−606.

(40) Kawabata, A. Electronic properties of fine metallic particles. III. E.S.R. absorption line shape. *J. Phys. Soc. Jpn.* **1970**, *29*, 902−911.

(41) Nistor, S. V.; Joita, A. C. Modular high-intensity monochromatic in situ illumination set-up for investigating ESR photoactive. *Appl. Magn. Reson.* **2020**, *51*, 287−296.

(42) Stoll, S.; Schweiger, A. EasySpin, a comprehensive software package for spectral simulation and analysis in EPR. *J. Magn. Reson.* **2006**, *178*, 42−55.

(43) Egerton, R. F.*Electron Energy-Loss Spectroscopy in the Electron Microscope*, 3rd Edition, Springer: 2011, p. 203.

(44) Wentorf, R. H., Jr. Cubic form of boron nitride. *J. Chem. Phys.* **1957**, *26*, 956−957.

(45) 1998 JCPDS-International Center for Diffraction Data, file 87−0794.

(46) 1998 JCPDS-International Center for Diffraction Data, file 86−2265.

(47) Spaeth, J. M.; Overhof, H.*Point Defects in Semiconductors and Insulators*, Springer Series in Materials Science, vol. *51*, eds. R., Hull, R. M., Osgood; J., Parisi, Springer, 2003.

(48) Baranov, P. G.; von Bardeleben, H. J.; Jelezko, F.; Wachtrup, J.*Magnetic resonance of semiconductors and their nanostructures. Basic and Advanced Applications*, Springer Series in Materials Science, vol. *253*, Springer Verlag GmbH, Austria, 2017.

(49) Hughes, A. E.; Jain, S. C. Metal Colloids in ionic crystals. *Adv. Phys.* **1979**, *28*, 717−828.

(50) Kimura, K.ESR spectroscopy of colloidal metal surfaces and conduction electrons. In *Encyclopedia of Surface and Colloidal Science*; Marcel Dekker: 2002; pp. 1981−1992.

(51) Weil, J.; Bolton, J. R.*Electron Paramagnetic Resonance. Elementary Theory and Practical Applications*, 2nd ed.; Wiley −Interscience: 2007.

(52) Guskos, N.; Zolnierkiewicz; Guskos, A.; Typek, J.; Berczynski, P.; Dolat, D.; Mozia, S.; Aidinis, C.; Morawski, A. W. Magnetic resonance of co-modified (Co,N)-TiO$_2$ nanocomposites. *Nukleonika* **2015**, *60*, 411−416.

(53) Hung, C. H.; Lee, C. H.; Hsu, C. K.; Li, C. Y.; Karna, S. K.; Wang, C. W.; Wu, C. M.; Li, W. H. Unusually large magnetic moments in the normal state and superconducting state of Sn nanoparticles. *J. Nanopart. Res.* **2013**, *15*, 1905.

(54) Li, W.-H.; Wang, C. W.; Li, C. Y.; Hsu, C. K.; Yang, C. C.; Wu, C. M. Coexistence of ferromagnetism and superconductivity in Sn nanoparticles. *Phys. Rev. B* **2008**, *77*, No. 094508.

(55) Kimura, K.; Bandow, S. Quantum size effect observed in ultrafine magnesium particles. *Phys. Rev. B* **1988**, *37*, 4473−4481.

(56) Geoffrion, L. D.; Guisbiers, G. Quantum confinement: size on the grill. *J. Phys. Chem. Solids* **2020**, *140*, No. 109320.

(57) Saiki, K.; Fujita, T.; Shimizu, Y.; Sakoh, S.; Wada, N. Electron Spin Resonance in fine particles of metallic lithium. *J. Phys. Soc. Jpn.* **1972**, *32*, 447−450.

(58) Borel, J.-P.; Millet, J.-L. Conduction Electron Spin Resonance in small particles suspended in solid matrix. *J. Phys. Colloques* **1977**, *38*, C2-115−C2-119.

(59) Aschroft, N. W., Mermin, N. D.*Solid State Physics, Holt, Rinehart and Winston, New York,* 1976.

(60) Barnes, S. E. Theory of electron spin resonance of magnetic ions in metals. *Adv. Phys.* **1981**, *30*, 801−938.

(61) CODATA*Recommended values of the fundamental physical constants: 2018.* NIST SP-961 (May2019).

(62) Orton, J. W.*Electron Paramagnetic Resonance: An Introduction to Transition Group Ions in Crystals*; Iliffe Books Ltd.: London, 1968.

(63) Orbach, R. Spin-lattice relaxation in rare-earth salts. *Proc. R. Soc. London, Ser. A* **1961**, *264*, 458−484.

(64) Sako, T.; Paldus, J.; Diercksen, G. H. F. The energy level structure of low −dimensional multi-electron QDs. *Adv. Quantum Chem.* **2009**, *58*, 177−201.

(65) Son, N. T.; Goto, K.; Nomura, K.; Thieu, Q. T.; Togashi, R.; Murakami, H.; Kumagai, Y.; Kuramata, A.; Higashiwaki, M.; Koukitu, A.; Yamakoshi, S.; Monemar, B.; Janzén, E. Electron properties of the residual donor in unintentionally doped β-Ga_2O_3. *J. Appl. Phys.* **2016**, *120*, 235703.

(66) Vidal, J.; Zhang, X.; Stevanović, V.; Luo, J.-W.; Zunger, A. Large insulating gap in topological insulators induced by negative spin-orbit splitting. *Phys. Rev. B* **2012**, *86*, No. 075316.

(67) Bardeleben, H. J.; Cantin, J. L.; Mynbaeva, M.; Saddow, S. E.; Shishkin, Y.; Devaty, R. P.; Choyke, W. J. EPR studies of SiC/SiO_2 interfaces in n-type 4H- and 6H oxidized porous Si. *Proc. Electrochem. Soc.* **2003**, *2*, 39−51.

(68) Konchits, A. A.; Shanina, B. D.; Krasnovyd, S. V.; Yukhymchuk, V. O.; Hreshchuk, O. M.; Valakh, M. Y.; Skoryk, M. A.; Kulinich, S. A.; Belyaev, A. E.; Iarmolenko, D. A. Structure and electronic properties of biomorphic carbon matrices and SiC ceramic prepared on their basis. *J. Appl. Phys.* **2018**, *124*, 135703.